TECHNISCHE UNIVERSITÄT WIEN

Diplomarbeit

Ejection of substellar objects from accretion disks through stellar encounters

Ausgeführt am Institut für Astrophysik
der Universität Wien

unter der Anleitung von
Dr. Eduard Vorobyov
und
Univ.Prof. Dr. Manuel Güdel
Co-Betreuung durch PD Dr. Herbert Balasin

Eingereicht an der Fakultät für Physik
der Technischen Universität Wien

durch
Maria Steinrück, BSc.
Lindheimgasse 8/8
1140 Wien

Wien, am 28. Oktober 2015 (Maria Steinrück)

Abstract

Stars often form in dense cluster environments, in which encounters between young stars are likely. If such an encounter happens while one of the stars has an extended disk that is gravitationally unstable, fragments formed within the disk can be ejected via multi-body gravitational interaction. This might be a formation mechanism for free-floating brown dwarfs and giant planets. The thesis examines the viability of this scenario with the hydrodynamics code developed at the University of Vienna. It was found that the ejection of fragments, both of fragments formed in the disk before the encounter and of fragments formed in tidal tails during the encounter, is very likely in prograde encounters, but unlikely in retrograde encounters. In addition, in one of the simulations an FU Orionis-like outburst was observed when a fragment was accelerated onto the disk central star.

Kurzfassung

Sternhaufen sind aktive Zentren der Sternentstehung, wobei Annäherungen zwischen jungen Einzelsternen häufig stattfinden. Findet eine solche Annäherung zwischen Partnern statt, bei denen einer über eine Akkretionsscheibe verfügt, die gravitationelle Instabilitäten aufweist, so können Fragmente, welche sich in der Scheibe gebildet haben, dieser entrissen werden. Dies stellt einen möglichen Mechanismus zur Enstehung ungebundener brauner Zwerge und Riesenplaneten dar. Die Diplomarbeit untersucht dieses Szenario unter Verwendung eines an der Universität Wien entwickelten Computerprogramms für hydrodynamische Simulationen. Es zeigte sich, dass in Begegnungen mit prograden Orbits häufig Fragmente aus der Scheibe herausgeschleudert werden, oder in durch Gezeitenkräfte verursachten Spiralarmen entstehen und dann das System verlassen. Bei retrograden Orbits ist das Herausschleudern von Fragmenten unwahrscheinlich. Zusätzlich wurde in einer Simulation ein FU Orionis-Ausbruch beobachtet, der von einem Fragment, das auf den Stern im Zentrum der Scheibe geschleudert wurde, verursacht wurde.

Acknowledgments

First and foremost, I would like to thank my advisor Eduard Vorobyov. Looking back at the experiences my colleagues and I had in the course of our Bachelor's thesis, Master's thesis and the two smaller research projects required in the curriculum, I have come to the conclusion that it is not easy to design a good research project at this level from which both the student and the advisor benefit. The ideal project should be well-defined, but also leave some freedom to the student. It should challenge the student, but not completely overwhelm them. At the same time, if possible, the advisor's research group should also benefit from the project. In the best case, the student's research actually represents a contribution to expanding scientific knowledge. With this in mind, I should say that Eduard did an amazing job as advisor. I really enjoyed working on this project and am confident that I also learned a lot in this time.

In addition, I am very grateful to Prof. Manuel Güdel for letting me work in his research group and adopting the role of the official advisor and examiner at the defense, as well as to PD Dr. Herbert Balasin for co-advising the thesis and thus making it possible to do my thesis project at the Institute for Astrophysics at the University of Vienna. I would like to mention Philipp Löschl and Roman Ferstl, who shared an office with me, as well. We shared many interesting and helpful discussions in the past ten months. I would also like to thank my parents for their support during my studies and my whole family for proofreading my thesis one last time before I turned it in.

Though not directly related to the thesis, I want to express my thanks to everyone who helped me with the graduate school application process through advice, recommendation letters or proofreading my personal statements. I am incredibly excited about the program and the research group in which I am soon going to start working towards my PhD.

Contents

Chapter 1

Introduction

When a star forms through the collapse of a cloud core, infalling gas with high angular momentum from the outer regions of the cloud core forms an accretion disk around the protostar. If this disk becomes sufficiently massive and extended, gravitational instability leads to fragmentation, forming objects typically in the mass range of giant planets and brown dwarfs (Boss, 2001; Stamatellos and Whitworth, 2009). The majority of these fragments, however, migrates onto the star or are disrupted through tidal forces . Only few fragments can survive in a stable orbit, forming giant planet and brown dwarf companions (Vorobyov and Basu, 2010a; Zhu et al., 2012), or be ejected from the disk via multi-body interactions involving other fragments and form free-floating brown dwarfs (Basu and Vorobyov, 2012).

It might be important, though, to consider that stars do not form in isolation but in associations or clusters. Especially in dense young clusters, stars are likely to experience encounters with other stars. Thies et al. (2010) estimated that, assuming that massive protostellar disks exist for around 1 Myr, for an average $0.5\,M_\odot$ star in an ONC-type cluster the probability to experience an encounter with a periastron radius below 500 AU while hosting a massive disk is $\approx 9\%$. Encounters can significantly influence the evolution of protostellar disks, which has been confirmed by numerical studies which combine cluster simulations with simulations of individual encounters (e.g. Pfalzner et al., 2008; Pfalzner, 2008; Rosotti et al., 2014). Among the expected effects are the truncation of disks and enhanced accretion rates. In addition, various more detailed simulations of individual encounters have been performed (e.g. Shen and Wadsley, 2006; Shen et al., 2010; Forgan and Rice, 2009, 2010; Thies et al., 2010; Muñoz et al., 2015), investigating the role of encounters in FU Orionis outbursts, brown dwarf formation, disk instability, truncation of disks and binary capture. A summary of studies focusing on brown dwarf formation is given in subsection 2.2.2.

None of these studies, however, considered encounters which involved a disk that was already gravitationally unstable before the encounter. Encounters involving fragmenting disks can be more complex, as the approaching star does not only interact with the disk, but also with the fragments. This might lead to the ejection of fragments formed in the disk before the encounter. In this thesis, this scenario is explored with numerical hydrodynamics simulations.

The thesis is organized as follows: chapter 2 reviews the theoretical background of disk fragmentation and brown dwarf formation. The numerical code used is described in chapter 3 and the results are presented and discussed in chapter 4. Chapter 5 then summarizes the findings.

Chapter 2

Motivation

2.1 Disk fragmentation

2.1.1 Criteria for fragmentation

A well-established necessary criterion for gravitational instability in disks is the Toomre criterion

$$Q = \frac{c_s \kappa}{\pi G \Sigma} < Q_{crit}, \tag{2.1}$$

where c_s is the speed of sound, κ the angular velocity, which for Keplerian disks can be replaced by the angular velocity Ω, G the gravitational constant and Σ the surface density. Q_{crit} is some value of order unity. The criterion was first derived by Toomre (1964) in the context of galactic disks, but applies to accretion disks as well. Its physical meaning can be understood qualitatively by considering a small density perturbation in the disk with radius ΔR. For small radii $\Delta R \lesssim c_s^2/G\Sigma_0 = \Delta R_l$, pressure prevents the area from collapsing. For large radii $\Delta R \gtrsim G\Sigma_0/\Omega^2 = \Delta R_u$ the area is stabilized by rotation. Thus, a perturbation can only grow if its characteristic length scale is larger than ΔR_l but smaller than ΔR_u. Now if $\Delta R_u < \Delta R_l$, there is no regime in which an instability can grow and the disk is stable against rotation. Solving the inequality then gives the Toomre criterion with $Q_{crit} = 1$.

The exact value of Q_{crit} can be obtained through a more thorough stability analysis and depends on the physical situation considered, e.g. whether the disk can be assumed to be infinitely small or has a finite thickness, and whether one considers a fluid or a sheet of stars (cf. Binney and Tremaine, 1987).

Another necessary condition for disk fragmentation is that the cooling time τ_c is smaller than a few times the local dynamical time scale Ω^{-1} (Gam-

mie, 2001; Rice et al., 2003),

$$\tau_c \lesssim 3\Omega^{-1}. \tag{2.2}$$

If the Toomre criterion is fulfilled but the cooling time is too large, regions with enhanced density cannot cool fast enough to collapse and form fragments. Instead, the disk settles into a quasi-stable state in which heating through dissipation of turbulence driven by the instability is balanced by cooling.

2.1.2 Implications of disk fragmentation

Disk fragmentation typically happens in the early evolution of a disk, when the protostar is still embedded in an envelope of gas from its parent cloud core. As material from the envelope keeps falling onto the disk, the surface density grows until the disk becomes gravitationally unstable and fragments. Only sufficiently massive and extended disks reach this unstable phase. Whether a disk will go through a phase of fragmentation therefore depends on the initial conditions of the cloud core, specifically on its initial mass and the ratio of rotational to potential energy β.

Fragments migrating inward and falling onto the star can cause sharp peaks in the accretion rate and thus lead to a luminosity burst of the same order of magnitude as FU Orionis-type bursts. (Vorobyov and Basu, 2005, 2006)

In addition, disk fragmentation has been invoked to explain the formation of giant planets, brown dwarfs and low-mass stars on wide (tens to hundreds of AU) orbits (e.g. Boss, 2001; Stamatellos and Whitworth, 2009; Kratter et al., 2010a,b; Vorobyov and Basu, 2010a; Vorobyov, 2013). The recent discovery of extrasolar giant planets on wide orbits through direct imaging has led to an increased interest in giant planet formation through gravitational instabiliy, as the standard theory for the formation of giant planets, core-accretion, fails to explain their formation: At such wide separations from the star, the dust density is too low for cores to grow within the disk life-time. However, analytical arguments (Kratter et al., 2010b) and numerical simulations (Stamatellos and Whitworth, 2009) show that the majority of objects formed through disk fragmentation have masses in the brown dwarf and low-mass star regimes. If these planets formed through disk fragmentation, they are the low-mass tail of the distribution of objects formed in the disk.

One problem of this formation scenario is the unlikely survival of fragments: Though disk fragmentation forms objects in all disks that are massive and extended enough, the majority of these objects is either driven onto the

star due to torques from spiral arms and other fragments or torn apart by tidal forces (Vorobyov and Basu, 2010a; Zhu et al., 2012). It seems that only fragments forming at the very end of the phase of disk fragmentation and are massive enough to open a gap in the disk have a chance to survive in a stable orbit. Vorobyov (2013) showed that this typically happens only in the most massive and extended disks, which are still unstable in the early T Tauri phase, after infall from the envelope has ceased. In some cases, fragments can also be ejected from disks through gravitational multi-body interactions and form free-floating brown dwarfs (Basu and Vorobyov, 2012).

2.2 Brown dwarf formation

2.2.1 Definition and general properties

Brown dwarfs are substellar objects below the hydrogen burning limit ($\approx 0.075\,\mathrm{M}_\odot$). The definition favored by the IAU and used by most authors sets the deuterium burning limit at $\approx 0.012\,\mathrm{M}_\odot$ as the lower mass limit for an object to be classified as brown dwarf. However, deuterium burning only has a small impact on the evolution of substellar objects. This, and recent discoveries of objects below the deuterium burning limit whose properties and formation seem to be better explained by counting them to the low-mass end of the brown dwarf population than by considering them giant planets, have led some authors to question this definition (Luhman, 2012; Chabrier et al., 2014). Instead, they suggest a distinction based on the dominant formation mechanism. The majority of giant planets are expected to form via core-accretion, while the question of the formation mechanism for brown dwarfs is not settled yet (see Section 2.2.2). Within this thesis, I will stick to the traditional definition for simplicity and distinguish between brown dwarfs and planetary-mass objects based on their masses. However, for the purpose of this thesis it is not crucial which definition is used.

Brown dwarfs are found in orbits around stars or other brown dwarfs as well as free-floating. Their spatial distribution and velocity dispersion in young clusters do not differ significantly from the ones of stars (Chabrier et al., 2014). A large fraction of young brown dwarfs have been observed to host accretion disks (Luhman, 2012, and references therein).

2.2.2 Formation scenarios

In a simplistic picture of star formation, a molecular cloud collapses to form a star if its self-gravity overcomes hydrostatic pressure. The minimum mass

required for collapse assuming a spherical cloud and a given constant density and pressure is called the Jeans mass. Though in reality several other factors such as turbulence, non-uniform density and fragmentation of collapsing cores play a role, one would expect the mass of stars to be not much smaller than the Jeans mass. However, the Jeans masses for typical conditions in molecular clouds are much larger than the masses of brown dwarfs, raising the question how these objects could form.

The following scenarios have been proposed to explain the formation of brown dwarfs (see Chabrier et al., 2014; Luhman, 2012):

- Photoionization: In this scenario, the mass accretion onto protostars is halted by the photoionizing radiation of nearby massive OB stars, heavily truncating the initial mass reservoir in collapsing cores (Whitworth and Zinnecker, 2004).

- Accretion-ejection: Stellar embryos are ejected from their accretion reservoir through dynamical interactions in dense clusters (Reipurth and Clarke, 2001; Bate, 2012).

- Gravoturbulent fragmentation: Large-scale turbulence in molecular clouds induces turbulence at smaller scales and produces overdensities that collapse. In clouds dominated by turbulence, the mass spectrum depends on the Mach number. The Jeans mass then is no longer a good estimate for the characteristic mass of collapsing cloud cores. Theories of gravoturbulence are successful in explaining the shape of the core mass function (CMF) and can predict cores down to the brown dwarf regime. If these cores evolve into stars without significantly fragmenting and changing the mass function, the CMF is directly related to the initial mass function (IMF). In this case the theory can explain the formation of brown dwarfs, which then are just the low-mass tail of the normal star formation process.

- Disk fragmentation (see Section 2.1): Though most fragments in gravitationally unstable disks migrate onto the star or are disrupted through tidal forces, simulations show that under certain conditions fragments can survive and form quasi-stable orbits around their star (Vorobyov, 2013; Zhu et al., 2012). Fragments can also be ejected from disks via multi-body interaction to form free-floating brown dwarfs (Basu and Vorobyov, 2012).

Observations place some constraints on these scenarios. As the brown dwarf mass function appears to be independent of the presence of O and B

stars, photoionization can be ruled out as a dominant formation mechanism. The observation of isolated protostellar objects with masses in the brown dwarf regime, with some of them having an accretion reservoir too small to grow above the hydrogen-burning limit, suggests that brown dwarfs can form without dynamical ejections from high-density regions or the presence of protostellar disks. This favors the gravoturbulent scenario, though Basu and Vorobyov (2012) argue that the ejection of clumps that have not yet collapsed instead of finished brown dwarfs could explain these isolated proto-brown dwarfs as well. However, as mentioned above, the gravoturbulent scenario can explain brown dwarf formation only if the distribution of stellar masses is mainly determined through the CMF. This requires that other processes such as dynamical interactions, competitive accretion or radiative feedback from other stars only play a minor role in determining the IMF. Whether this is the case is subject to on-going debate (Offner et al., 2014).

It is quite possible that brown dwarfs can form through several of the proposed mechanisms, with each of them contributing to the total number of brown dwarfs. The reviews of Chabrier et al. (2014) and Luhman (2012) both conclude that though observations suggest that at least some brown dwarfs are just the low-mass tail of star formation formed though gravoturbulent fragmentation, it is premature to rule out that other formation mechanisms such as disk fragmentation or accretion-ejection contribute to the total number of brown dwarfs as well.

2.2.3 Formation through stellar encounters

A problem of the disk fragmentation scenario is that massive, extended disks that fragment appear to be rare. However, most disk mass measurements are restricted to the optically visible, late T Tauri stage. In the early embedded stage, massive disks may be a rule rather than an exception. As Figure 1 in Vorobyov (2013) shows, out of the disks which experience fragmentation, only the more massive and extended ones can eject fragments, as this requires the presence of at least two relatively massive fragments at the same time. An even smaller fraction is expected to form brown dwarfs or giant planets on stable orbits. However, it has been suggested that stellar encounters could trigger fragmentation (e.g. Thies et al., 2010). Similarly, encounters could enhance fragmentation in already unstable disks. They could also lead to the ejection of fragments formed in the disk before the encounter.

Shen et al. (2006; 2010) simulated encounters of large, extended protostellar disks. They found that encounters were likely to produce fragments spanning mass ranges from planetary-mass objects to low-mass stars. A large fraction of the fragments were unbound at the end of the simulations. How-

ever, disks as large and massive as in their simulations ($M_d = 0.6\,\mathrm{M}_\odot, r \approx 1000\,\mathrm{AU}$) are rare (even in the embedded phase) and it seems unlikely that two such massive disks collide. A more likely scenario is an encounter involving two smaller disks, or an encounter of a massive disk with a star that has a small disk or no disk at all. Forgan and Rice (2009) studied the effect of a close encounter with a low-mass star on a marginally stable disk. In their simulations compressive and shock heating stabilized the disk against fragmentation. Their study focused on encounters with periastron radii $\leq 50\,\mathrm{AU}$. Such close encounters, however, are unlikely. In contrast, Thies et al. (2010) found that encounters were able to trigger fragmentation in marginally stable disks and thus form objects between $0.01\,\mathrm{M}_\odot$ and $0.16\,\mathrm{M}_\odot$. They were using larger disks ($M_d \approx 0.5\,\mathrm{M}_\odot, r \lesssim 500\,\mathrm{AU}$) and more distant (400-500 AU) encounters.

None of the above mentioned studies considered accretion disks that are already unstable and host fragments. However, encounters in such disks might be more complex. In addition to fragments formed through the encounter, already existing fragments could be ejected, increasing the efficieny of brown dwarf formation. Existing fragments could also be driven onto one of the stars, causing luminosity bursts.

In our simulations, we consider a gravitationally unstable disk with a mass of $0.25\,\mathrm{M}_\odot$ around a $0.63\,\mathrm{M}_\odot$ star in the embedded phase of star formation, during which the disk still experiences significant infall of material from the envelope. The initial configuration of the disk and surrounding envelope was obtained through the self-consistent simulation of a collapsing cloud core (see Section 4.1). The disk is then approached by a more massive ($1.2\,\mathrm{M}_\odot$) intruding star without a disk. The choice of a more massive star increases the strength of the interaction with the disk.

Though the main reason for neglecting the disk of the intruder is restrictions of our numerical model, the situation that one of the stars has no disk or only a small disk is probably not unrealistic: Observations of young clusters show a large spread in luminosity (Hillenbrand, 2009). As the age of pre-main sequence stars is typically determined by placing stars on the Hertzsprung-Russel diagram (HRD) and comparing their position to evolutionary tracks derived from theoretical models, this luminosity spread has often been interpreted as an age spread of up to 10 Myr. It is likely that a large part of the luminosity spread can be explained by uncertainties in deriving the position on the HRD and systematic errors of the evolutionary models (Hillenbrand, 2009). However, Da Rio et al. (2010) found in a careful analysis including these uncertainties that they still needed an age spread of 2.8-4 Myr to explain the data from young association LH 95 in the Large Magellanic Cloud. In contrast, Slesnick et al. (2008) found that data from the

Upper Scorpius association was consistent with all stars forming at the same time after correcting for uncertainties, even though a naive interpretation of the HRD would yield an age spread $> 10\,\mathrm{Myr}$. Nevertheless, they could not rule out an age spread below 6 Myr. The average life time of protostellar disks is estimated to be 2-3 Myr. Thus, it is quite possible that one of the stars involved in the encounter has a massive disk, while the disk of the other star has already been cleared.

Chapter 3

Code

3.1 Hydrodynamics code

In this section, the main features of the hydrodynamics code used for the simulations are summarized. A more detailed description of the code can be found in Vorobyov and Basu (2006, 2010b, 2015). The code was developed to be able to self-consistently model the collapse of a cloud core over a few Myr from the pre-stellar phase through the embedded phase of star formation to the T Tauri phase. In the embedded phase of star formation, star and disk are formed and gas continues to fall onto the disk from the surrounding envelope. Thus, the computation domain is chosen large enough to include the infalling envelope: the outer boundary is set to 0.07 parsec. The inner boundary is a sink cell at a radius of 8 AU. The sink cell is introduced to avoid too small time steps and is dynamically inactive but does contribute to the gravitational potential of the disk. We assume that 90 % of the gas flowing into the sink cell is eventually accreted to the central star, while the other 10 % are lost in protostellar jets.

The code solves the hydrodynamics equations in the thin-disk approximation. In thin disks ($Z/r \ll 1$, where Z is the vertical scaleheight of the disk and r the radius) the gas is supported by hydrostatic pressure in the z-direction and rotates with a roughly Keplerian speed around the central star (see e.g. Longair, 2011, chap. 14). Thus, it is reasonable to assume that the velocity of the gas is independent of the z-component. Integrating the hydrodynamics equations for mass, momentum and energy over the z-component

then gives

$$\frac{\partial \Sigma}{\partial t} = -\nabla_p \cdot (\Sigma \boldsymbol{v}_p), \tag{3.1}$$

$$\frac{\partial}{\partial t}(\Sigma \boldsymbol{v}_p) + [\nabla \cdot (\Sigma \boldsymbol{v}_p \otimes \boldsymbol{v}_p)]_p = -\nabla_p \mathcal{P} - \Sigma \nabla_p (\Phi_* + \Phi_{disk} + \Phi_{intr} + \Phi_{ind}) + (\nabla \cdot \boldsymbol{\Pi})_p, \tag{3.2}$$

$$\frac{\partial e}{\partial t} + \nabla_p \cdot (e \boldsymbol{v}_p) = -\mathcal{P}(\nabla_p \cdot \boldsymbol{v}_p) - \Lambda + \Gamma + (\nabla \boldsymbol{v})_{pp'} : \boldsymbol{\Pi}_{pp'}, \tag{3.3}$$

where subscripts p and p' denote the planar components (r, ϕ) in polar coordinates. Σ is the mass surface density, $\boldsymbol{v}_p = v_r \hat{\boldsymbol{r}} + v_\phi \hat{\boldsymbol{\phi}}$ is the velocity in the disk plane and $\mathcal{P} = \int_{-Z}^{Z} P dz$ is the vertically integrated gas pressure, which is calculated using the equation of state for an ideal gas $\mathcal{P} = (\gamma - 1)e$, with e being the internal energy per surface area. The ratio of specific heats γ is assumed to be

$$\gamma = \begin{cases} 5/3 & \text{if } T < 100\,\text{K} \\ 7/5 & \text{if } 100\,\text{K} < T < 2000\,\text{K} \\ 1.1 & \text{if } T > 2000\,\text{K}. \end{cases} \tag{3.4}$$

The terms contributing to the total potential are the gravitational potential of disk central star Φ_*, the self-gravity of the disk Φ_{disk}, the potential of the intruder Φ_{intr} and the indirect potential Φ_{ind}. The self-gravity of the disk is calculated via a Fast Fourier Transformation solving the Poisson Integral

$$\Phi_{disk} = -G \int_{r_{sc}}^{r_{out}} r' dr' \int_0^{2\pi} d\phi' \, \frac{\Sigma(r', \phi')}{\sqrt{r'^2 + r^2 - 2rr' \cos(\phi' - \phi)}}. \tag{3.5}$$

The potential of the intruder is given by equation 3.17. As the center of the coordinate system is moving with the central star, non-inertial accelerations have to be taken into account. The acceleration of the central star, and thus of the coordinate system, is given by

$$\boldsymbol{g}_* = G \int \frac{dm(\boldsymbol{r'})}{r'^3} \boldsymbol{r'} + G \frac{M_{intr}}{r_{intr}^3} \boldsymbol{r}_{intr}, \tag{3.6}$$

where $dm(\boldsymbol{r'})$ is a mass element in the disk with position vector $\boldsymbol{r'}$, M_{intr} is the mass of the intruder and $\boldsymbol{r_{intr}}$ is the position vector of the intruder. The term that has to be added to the total gravitational acceleration thus is $-\boldsymbol{g}_*$.

This term can be expressed as the derivative of a potential, the so-called indirect potential $\Phi_{ind} = \boldsymbol{r} \cdot \boldsymbol{g}_*$. As the derivative in equation 3.2 is taken with respect to $\boldsymbol{r}$ and the potential depends only on $\boldsymbol{r'}$ and $\boldsymbol{r}_{intr}$, the right behavior is reproduced.

The viscous stress tensor is represented by Π. The expressions for the divergence of the stress tensor $(\nabla \cdot \boldsymbol{\Pi})_p$, the symmetrized velocity gradient tensor $(\nabla \boldsymbol{v})_{pp'}$ and the viscous heating term $(\nabla \boldsymbol{v})_{pp'} : \boldsymbol{\Pi}_{pp'}$ in polar coordinates can be found in Vorobyov and Basu (2010b).

Viscosity is treated using the α-prescription (Shakura and Sunyaev, 1973)

$$\nu = \alpha c_s Z, \tag{3.7}$$

where c_s is the speed of sound. In this work, α is set to 0.01, which is within the range expected from simulations of the magneto-rotational instability.

Heat transport is considered only in the form of radiation, other possible mechanisms such as convection are neglected. Radiation escapes at the surface of the disk at a rate per unit area $2\sigma T_{eff}^4$, where σ is the Stefan-Boltzmann constant. Using the diffusion approximation, in the optically thick limit the effective temperature is linked to the midplane temperature T_{mp} via $T_{eff}^4 = 8/(3\tau) T_{mp}^4$ with the optical depth τ (Johnson and Gammie, 2003). In the optically thin limit, the cooling function is $2\sigma T_{mp}^4 \tau$. Thus, the expression for the cooling function that links both regimes is

$$\Lambda = \mathcal{F}_c \sigma T_{mp}^4 \frac{\tau}{1+\tau^2}, \tag{3.8}$$

where $\mathcal{F}_c = 2 + 20 \tan^{-1}(\tau)/(3\pi)$ is a function that ensures a smooth transition between the optically thick and the optically thin regime. The heating function is given by

$$\Gamma = \mathcal{F}_c \sigma T_{irr}^4 \frac{\tau}{1+\tau^2}, \tag{3.9}$$

with the irradiation temperature T_{irr} defined as

$$T_{irr}^4 = T_{bg}^4 + \frac{F_{irr}(r)}{\sigma}. \tag{3.10}$$

The uniform background temperature T_{bg} is set to 10 K. The flux from the central star absorbed by the disk at a radius r with the incidence angle of the radiation arriving at the disk surface γ_{irr} is

$$F_{irr}(r) = \frac{L_*}{4\pi r^2} \cos \gamma_{irr}. \tag{3.11}$$

The luminosity L_* is the sum of the photospheric luminosity L_{ph} and the accretion luminosity $L_{accr} = (1-\epsilon) G M_* \dot{M}/(2R_*)$, where ϵ is the fraction

of the accretion energy absorbed by the star. This fraction is taken to be $\epsilon = 0$ as long as $\dot{M} < 10^{-5}\,\mathrm{M}_\odot\,\mathrm{yr}^{-1}$ and $\epsilon = 0.2$ if the accretion rates rises above $10^{-5}\,\mathrm{M}_\odot\,\mathrm{yr}^{-1}$ (see Baraffe et al., 2012). The stellar radius R_* and L_{ph} are calculated by the stellar evolution code described in Baraffe and Chabrier (2010). Remarks on the coupling between the hydrodynamics code and the stellar evolution code can be found in Vorobyov and Basu (2015). The luminosity of the intruder is currently not taken into account.

Equations (3.1)-(3.3) are solved on a polar 512 x 512 grid with logarithmic cell spacing in the radial direction. At the inner boundary, free outflow boundary conditions are imposed, which allow matter to flow out from the computation domain, but prevent inflow. For the outer boundary free outflow conditions, as used in previous simulations, are problematic. As the coordinate system moves with the central star, which is accelerated towards the intruder, but the mass close to the boundary remains largely unaffected by this acceleration, large amounts of mass leave the simulation domain in the direction opposite to the acceleration. Meanwhile, in the direction of the acceleration no material can enter the simulation domain, which leads to the creation of artificial low-density regions causing the code to crash. Therefore, free boundary conditions that allow for both inflow and outflow are used at the outer boundary. Details of the numerical solution procedure can be found in Vorobyov and Basu (2010b).

3.2 Intruder

For the scope of this thesis, the motion of the intruder is restricted to the disk plane. Coplanar encounters are expected to have the highest impact on the disk and our numerical code is best suited for this type of encounters. The equations of motion for a particle moving in a gravitational potential Φ in polar coordinates, written as first order differential equations, are given by

$$\dot{r} = v_r, \tag{3.12}$$

$$\dot{\varphi} = \frac{v_\varphi}{r}, \tag{3.13}$$

$$\dot{v}_r = \frac{v_\varphi^2}{r} + a_r, \tag{3.14}$$

$$\dot{v}_\varphi = -\frac{v_\varphi v_r}{r} + a_\varphi, \tag{3.15}$$

with the acceleration calculated as

$$\boldsymbol{a} = -\nabla(\Phi_* + \Phi_{ind}) + \frac{1}{M_{intr}} \sum_{j,k} \boldsymbol{F}_{j,k}, \tag{3.16}$$

where $\boldsymbol{F}_{j,k}$ is the force the intruder experiences from a single grid cell, given in equation (3.18), and the summation is performed over all grid cells. To calculate the trajectory of the intruder, equations (3.12)-(3.15) are solved using a Dormand-Prince method (a fifth-order Runge-Kutta method) with adaptive stepsize control (see Press et al., 2007, chap. 17.2). Several tests performed to demonstrate that the code is producing correct results are described in Appendix A.

3.2.1 Intruder-Disk interaction

To calculate the influence of the intruder on the gas in the disk, the gravitational potential of the intruder is added to the total potential on each grid point in the hydrodynamics code. The potential at a grid cell with indices j and k is given by

$$\Phi_{intr}(R_{j,k}) = \begin{cases} -GM_{intr}/R_{j,k} & \text{for } R_{j,k} > r_s \\ \Phi_{smooth} & \text{for } R_{j,k} < r_s, \end{cases} \tag{3.17}$$

where r_s is the smoothing radius and Φ_{smooth} is given by equation (3.19). The symbol $\boldsymbol{R}_{j,k} = \boldsymbol{r}_{j,k} - \boldsymbol{r}_{intr}$ is used for the vector pointing from the intruder towards the center of the grid cell and the distance between the intruder and the distance between the grid cell and the intruder is denoted by $R_{j,k} = |\boldsymbol{R}_{j,k}|$.

3.2.2 Disk-Intruder interaction

The force that the disk exerts onto the intruder is calculated by summing the contributions from each cell, treating the cells as point masses with mass $M_{j,k}$. The contribution from an individual cell is given by

$$\boldsymbol{F}_{j,k} = \begin{cases} \dfrac{GM_{intr}M_{j,k}}{R_{j,k}^3}\boldsymbol{R}_{j,k} & \text{for } R_{j,k} > r_s \\ \boldsymbol{F}_{j,k}^{(smooth)} & \text{for } R_{j,k} < r_s, \end{cases} \tag{3.18}$$

with $\boldsymbol{F}_{j,k}^{(smooth)}$ defined in equation (3.20). As the summation is computationally expensive, the forces are updated only once per hydrodynamical timestep.

3.2.3 Gravitational softening

The gravitational forces between the gas and the intruder can become extremely strong if the intruder approaches one of the cell centers, where all

mass is concentrated according to our convention. To avoid this unphysical behavior, the potential has to be modified for small distances. We use the same potential as in Klahr and Kley (2006), where the potential for distances smaller than a smoothing radius r_s is set to

$$\Phi_{smooth}(R_{j,k}) = -GM_{intr}\left(\frac{R_{j,k}^3}{r_s^4} - 2\frac{R_{j,k}^2}{r_s^3} + \frac{2}{r_s}\right). \tag{3.19}$$

At r_s the smoothed potential and its first and second derivatives agree with the unaltered potential $-GM_{intr}/R_{j,k}$ and its derivatives. The advantage of this choice is that it only modifies the potential for distances smaller than r_s, unlike the common approach $\Phi(R_{j,k}) = -GM/\sqrt{R_{j,k}^2 + r_s^2}$.

The modified force that a single grid cell with a distance from the intruder smaller than r_s exerts on the intruder is then given by

$$\boldsymbol{F}_{j,k}^{(smooth)} = GM_{intr}M_{j,k}\left(\frac{4}{r_s^3} - \frac{3R_{j,k}}{r_s^4}\right)\boldsymbol{R}_{j,k}. \tag{3.20}$$

The choice of the smoothing radius r_s is not trivial. If it is too small, the gravitational interaction of the gas and the intruder will be overestimated, a too large r_s will underestimate the forces. As the smoothing is introduced to compensate discretization effects, it seems plausible that the smoothing radius has to be related to the cell size:

$$r_s = q_s \cdot \min(\Delta r, r\Delta\phi), \tag{3.21}$$

where Δr and $\Delta\phi$ are the local cell spacings in the radial and azimuthal direction. Testing different smoothing radii shows that $q_s = 1$ results in unexpectedly strong interactions with the disk, altering the trajectory of the intruder more than expected, while there is relatively little difference between $q_s = 2$ and $q_s = 3$. We therefore choose $q_s = 3$ throughout the simulations.

Chapter 4

Simulations

4.1 Initial conditions and early disk evolution

To obtain a suitable initial condition, a simulation of the collapse of a cloud core was run, similar to the simulations in Vorobyov and Basu (2015). The total mass of the model is $1.08 M_{\odot}$ and the ratio of rotational to gravitational energy β is $6.2 \cdot 10^{-3}$. The initial surface density and angular velocity profiles are the same as in Vorobyov and Basu (2010b). After a pre-stellar collapse phase and the formation of a central star a centrifugal disk is formed. The envelope then falls onto the disk at a higher rate than the accretion of the disk onto the star, increasing the disk mass until the disk becomes gravitationally unstable. In the subsequent evolution, fragments form in the disk and migrate to the central star, causing luminosity bursts (Vorobyov and Basu, 2010b). We choose the configuration of the disk at a time during this disk unstable phase, at $t = 0.42$Myr, as initial setup for all simulations including the intruder. At this time, the central star has a mass of $0.63\,\mathrm{M}_{\odot}$ and the disk mass is $0.25\,\mathrm{M}_{\odot}$. The surface density inside 1000 AU at this time is plotted in Figure 4.1. The disk extends to around 600 AU from the central star and is gravitationally unstable. There is one fragment present in the disk to the left of the central star. At the top, at around 500 AU distance from the central star, an overdensity can be seen. Soon afterwards it collapses and forms a fragment.

The intruder, with a mass of 1.2 $M_{\odot}$, is then added to the simulation at a distance of 3,000 AU, far enough to avoid any effects from the sudden appearance of the intruder on the disk.

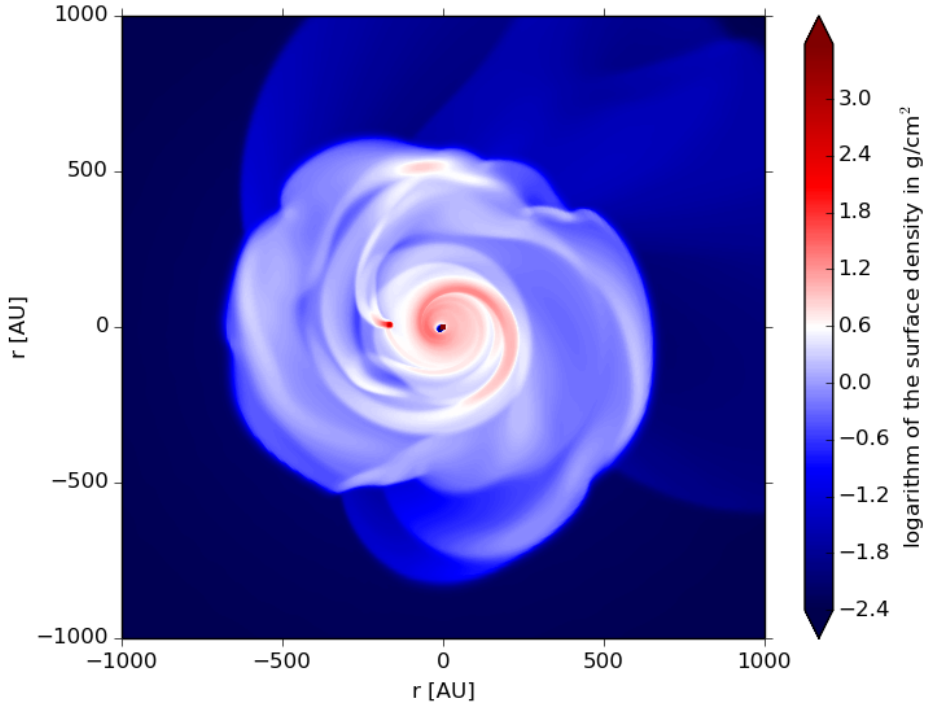

Figure 4.1: Surface density of the accretion disk at the time at which the intruder is added to the simulation. Only the region inside 1000 AU from the central star is shown.

4.2 Overview of the simulations

In total, I ran 16 simulations with different initial velocities and positions of the intruder. Half of the models have orbits corotating with the disk (prograde) and the other half are counterrotating (retrograde). Table 4.1 provides a summary of the initial conditions and results. The table shows both the periastron one would expect treating the disk and star as a point object and the actual periastron in the simulation. In most cases, the periastron in the simulation is lower than the expected value, due to gravitational torques from the disk and fragments in the disk and the capture of material by the intruder, forming a small disk. However, in a few cases, the intruder is accelerated by gravitational torques from fragments.

Table 4.2 shows the properties of the ejected fragments. Fragment masses and velocities were inferred using the fragment tracking algorithm described in Vorobyov (2013). Unless noted, the velocities and masses were determined at a distance of 3000 AU from the central star. To demonstrate that the fragments are really ejected, the ratio of kinetic to potential energy was calculated for each fragment in the center of mass frame (CM), the reference frame of the central star (S) (neglecting the intruder) and the reference frame of the intruder (I) (neglecting the central star). The lowest ratio for each fragment is given in the second column from the right.

4.3 Results

4.3.1 Ejection of existing fragments

In the majority of the prograde models, the fragment forming at the beginning of the simulation, before the intruder has approached the disk, is ejected from the disk due to three-body interaction. Figure 4.2 illustrates this process with a series of simulation snapshots from Model P1. Each panel shows the surface density in g/cm^2 on a logarithmic scale in a 4000 AU x 4000 AU box centered around the central star. In this figure, as well as in all other figures showing simulation snapshots, the position of the intruder is indicated by the intersection of the dotted lines. The position of the ejected fragment is highlighted by an arrow.

With only slight variations between different models, the mass of the ejected fragment is 20-25 Jupiter masses. An exception is Model P7 with 10 M_{Jup}, as the intruder passes the fragment relatively close, such that the fragment loses part of its mass. There is an additional amount of gas with 40-45 M_{Jup} (23 M_{Jup} in Model P7) located inside the Hill radius of the fragment.

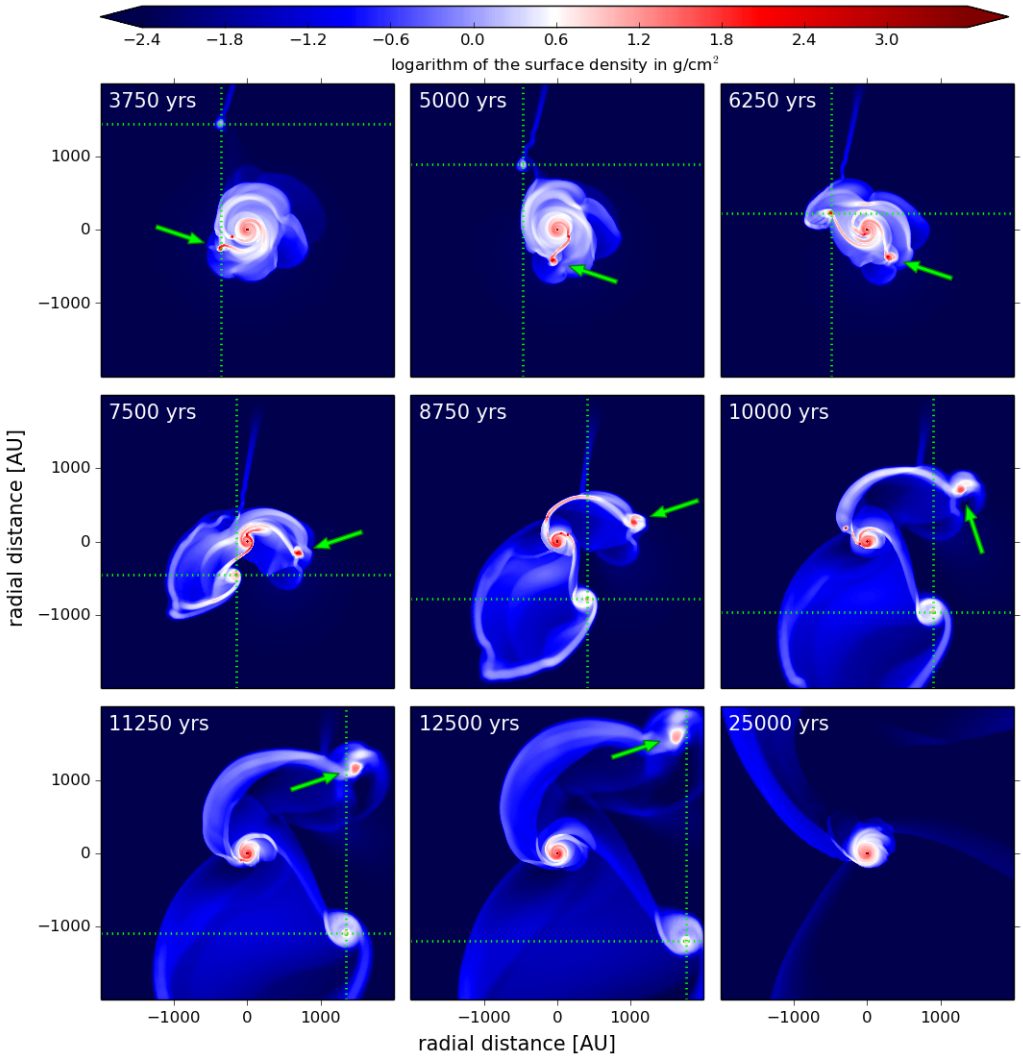

Figure 4.2: A series of simulation snapshots showing the ejection of a fragment from the disk through three-body interaction with the intruder and the central star in Model P1. The intersection of the dotted green lines marks the position of the intruder. The position of the fragment that is ejected is indicated with an arrow. The last panel shows the disk long after the encounter.

This mass is likely to be accreted by the fragment. Regardless of what fraction of the mass inside the Hill radius is accreted onto the fragment, its final mass is clearly in the brown dwarf regime. Thus, the fragment resembles a proto-brown dwarf. A fraction of the material in the Hill radius might become bound to the fragment and form a small accretion disk, as observed around some young brown dwarfs.

In most of the models in which the intruder has a retrograde trajectory, no ejections are observed. A spectacular exception is Model R1. In this model, the intruder passes the fragment very closely and catapults the fragment out of the system. The ejection process is illustrated in Figure 4.3, showing the surface density at six consecutive instances. In panel (a), the intruder approaches the fragment The closest approach, with a distance of $\approx 60\,\mathrm{AU}$, happens in panel (b). As can be seen in panels (c) and (d), the fragment gets highly distorted due to tidal forces and loses part of its mass. Once the intruder is well away, it returns to a roughly spherical shape (panels (e)-(f)).

At a radius of 3,000 AU from the central star, the fragment has a velocity of 2.1 km/s relative to the central star and 3.3 km/s relative to the intruder, significantly higher than the velocity of the other ejected fragments.

As the other simulations with the same initial position but different initial velocities show, this ejection event is rather a single lucky case than a robust general phenomenon.

4.3.2 Ejection of fragments formed in tidal arms

In several models (P4, P5, P6, P7, P8) fragments form in tidal arms formed during the encounter and are subsequently ejected. In Model P6 two clumps form in the same spiral arm close to each other and are ejected in the same direction. The formation of these two fragments can be seen in Figure 4.4, in which the surface density in a 4000 x 4000 AU box centered around the target star is plotted at four consecutive instances. The tidal arm in which the fragments form is indicated by an arrow. Due to the decreasing resolution of the grid they merge at a distance of $\approx$ 3000AU from the central star. However, a determination of the fragment masses, positions and velocities at $\approx$ 3000AU shows that they are not bound to each other. In Model R8 a fragment is formed in a tidal arm as well, however, its energy is not sufficient to leave the system.

With masses ranging from 5 to $13\,\mathrm{M_{Jup}}$ and gas masses located inside the Hill radius between 13 and $24\,\mathrm{M_{Jup}}$, the fragments formed in tidal arms are less massive than the fragments ejected from the disk. This is because they form at a larger distance from the star, where the temperatures are lower, corresponding to a lower Jeans mass. It is likely that the fragments will

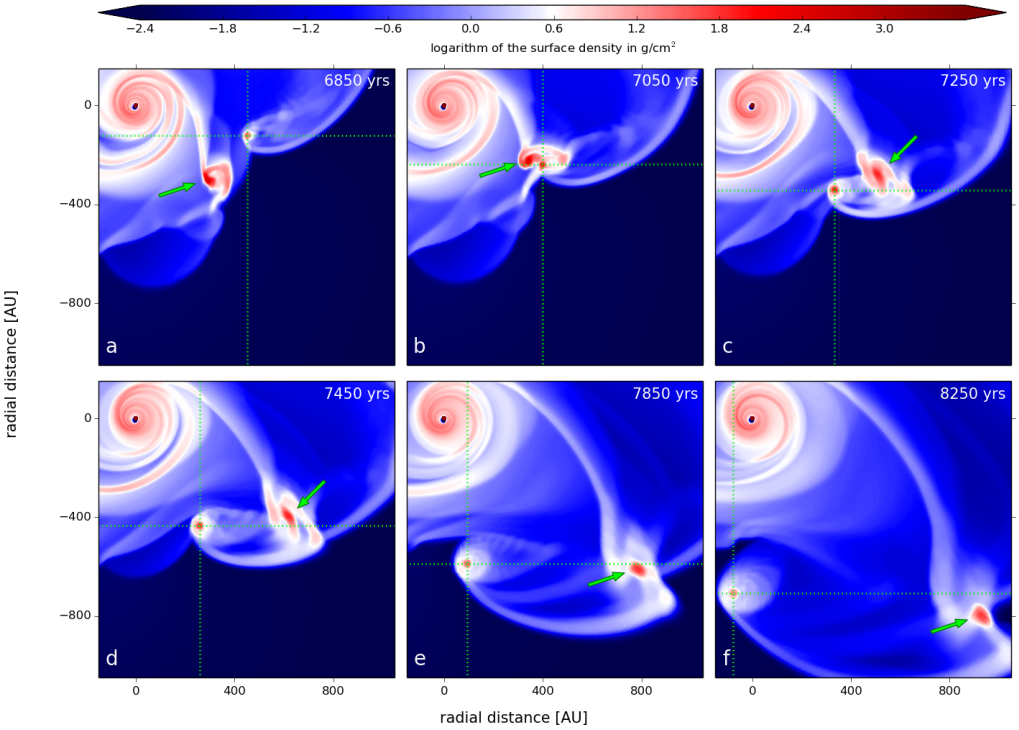

Figure 4.3: A series of simulation snapshots showing the ejection of the fragment through a close encounter between the fragment and the intruder in Model R1. Again, the position of the intruder is indicated by the intersection of the dotted green lines. The arrow highlights the position of the fragment.

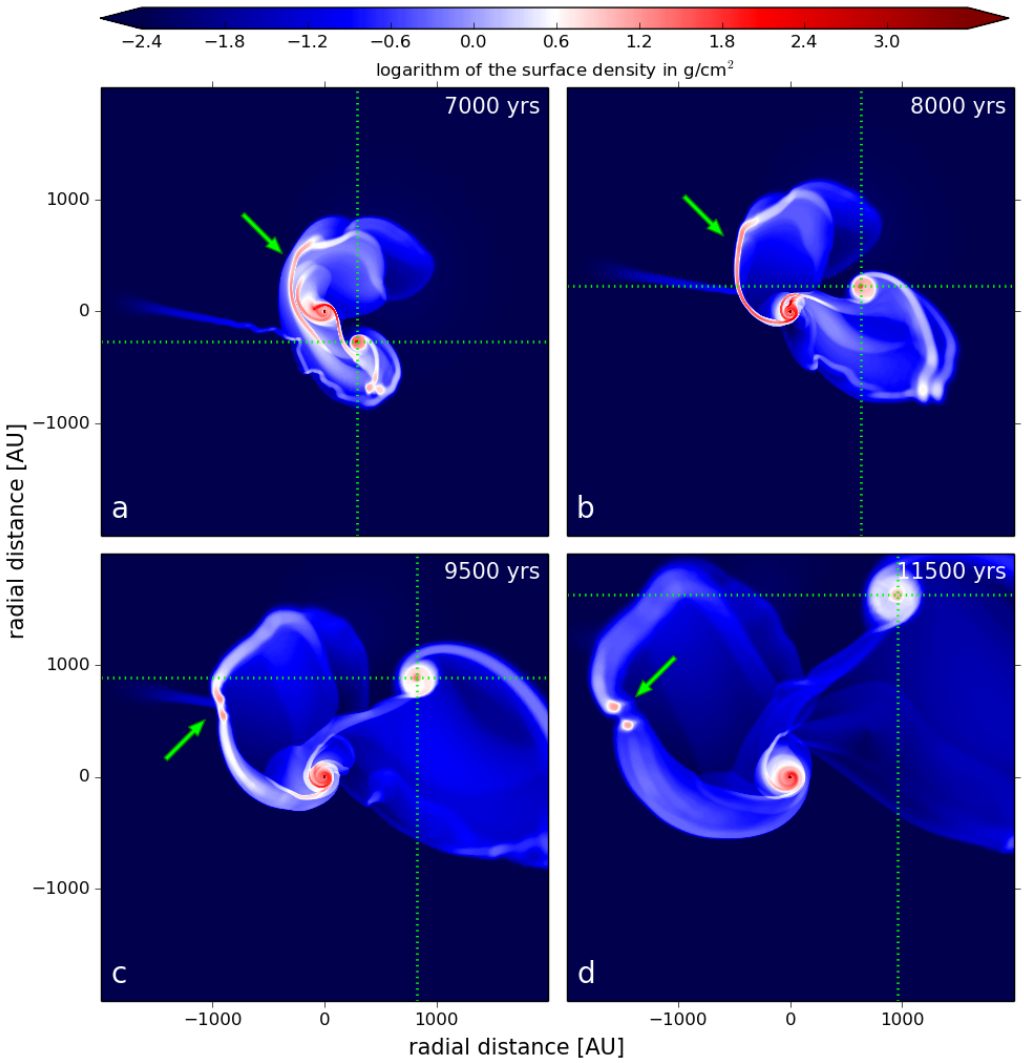

Figure 4.4: A series of simulation snapshots showing the formation of two fragments in a tidal arm in Model P6. Again, the position of the intruder is indicated by the intersection of the dotted green lines. The arrow highlights the tidal arm in which the fragments form.

accrete a fraction of the mass inside the Hill radius, though it is not clear how much exactly. Therefore, the fragments will form either low-mass brown dwarfs or free-floating planetary-mass objects.

All of the ejections of fragments formed in tidal arms happen in prograde encounters. This is because prograde encounters form more extended tidal structured, a behavior that has been observed in previous studies of encounters as well (e.g. Shen et al., 2010; Forgan and Rice, 2009).

4.3.3 Acceleration of a fragment onto the star - a cause for a FU Orionis outburst

In Model R5 the intruder passes the star just slightly inside the fragment. The close encounter with the intruder tears the fragment apart and accelerates it towards the central star. A series of snapshots of this event is shown in Figure 4.5. In panels (a) and (b) the fragment approaches the intruder. At its closest approach, tidal forces tear the fragment apart (panels (b) and (c)). The remains of the fragment are then accelerated towards the disk central star (panels (d) and (e)). When they hit the central star 7,800 years into the simulation, as seen in panel (f), a sharp increase in the accretion rate can be observed. Within less than 10 years[1], the accretion rate increases from $5 \cdot 10^{-7} M_{\odot} yr^{-1}$ to $3 \cdot 10^{-4} M_{\odot} yr^{-1}$. This rise would be observed as an FU Orionis (FUor) type outburst, for which accretion rates in the same order of magnitude are estimated (Hartmann and Kenyon, 1996; Audard et al., 2014). The accretion rate is plotted in Figure 4.6. In the left panel the evolution of the accretion rate throughout the whole simulation is displayed, while the right panel shows a close-up of the burst. After the sharp rise, the accretion rate declines until 200 years later a second spike, peaking at $6 \cdot 10^{-4} M_{\odot} yr^{-1}$, can be seen. A close examination of a sequence of simulation snapshots shows that the first peak is caused by remains of the fragment directly hitting the central star, while the second peak is caused by material initially passing the star, but then being quickly decelerated as it encounters the disk material head-on and subsequently falling onto the central star. After another 200 years, the accretion rate rapidly drops to its previous level. At $t \approx 8500\,\mathrm{yrs}$ more material, still from the disrupted fragment, falls onto the star and causes another, much smaller ($10^{-5} M_{\odot} yr^{-1}$), spike in the accretion rate.

[1]Note that the accretion rate is tracked only in 5-year steps. Because of this, and because the inner disk inside 8 AU is not included in the simulation domain, it is not possible to infer any meaningful statements on the behavior of the accretion rate on smaller timescales.

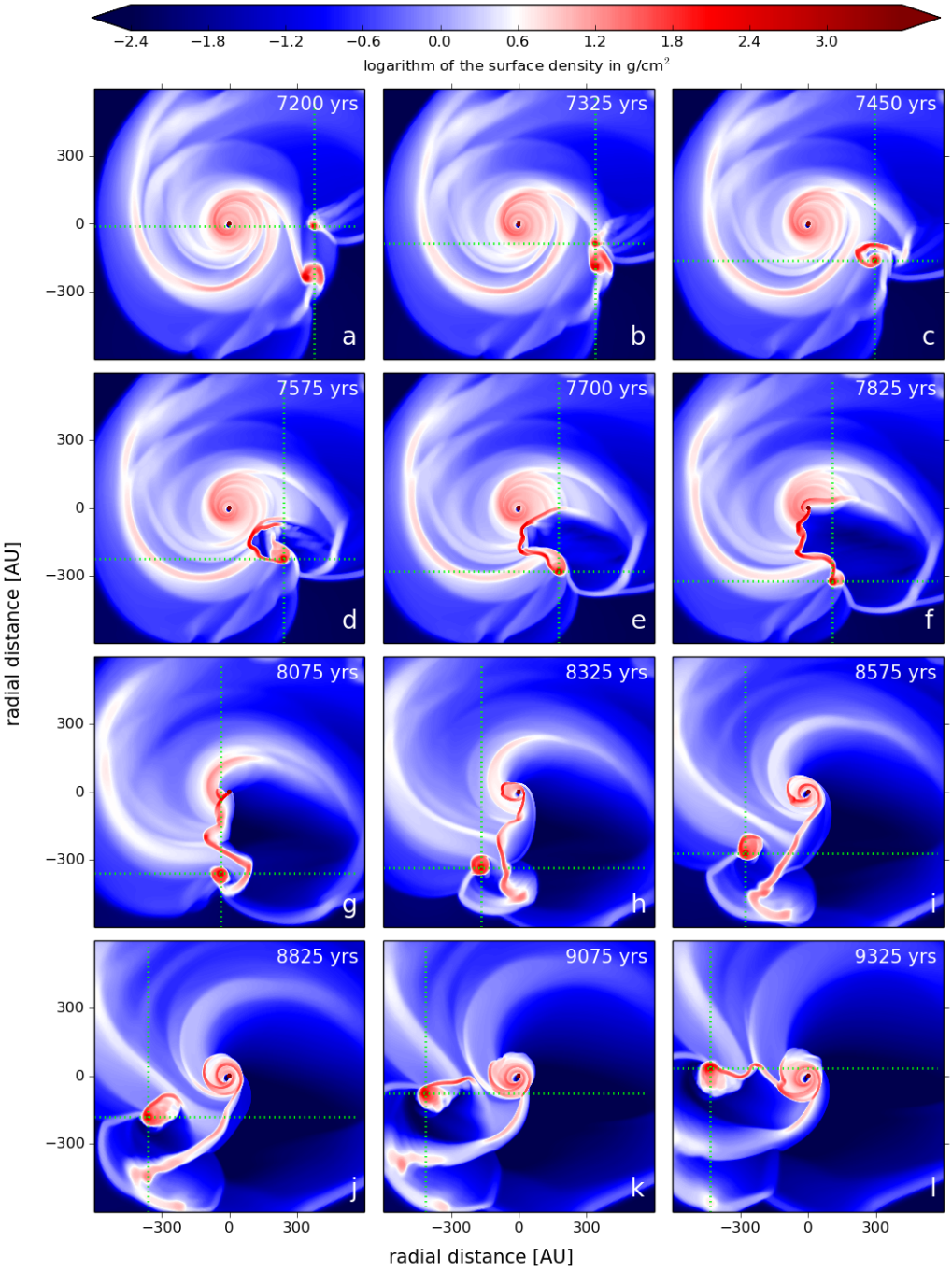

Figure 4.5: A series of simulation snapshots showing the acceleration of the fragment onto the central star in Model R5, causing an outburst. Note that the timespan between the snapshots is doubled in the bottom two rows.

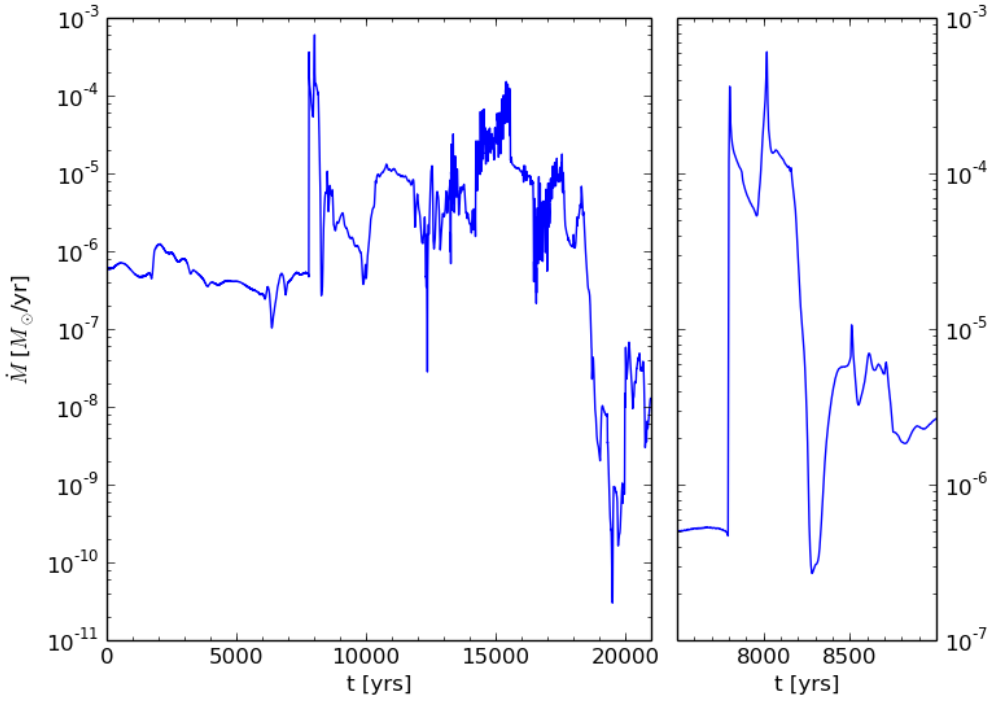

Figure 4.6: Accretion rate in Model R5. The accretion rate in the simulation is set equal to the gas flow into the central sink cell. The right panel shows the accretion rate during the outburst at $t = 7,800$ years in detail.

During the close encounter with the fragment, the intruder loses a significant amount of angular momentum and is thus caught by the central star. Until the end of the simulation, it completes two orbits. In this time, almost all of the disk material is either accreted by the intruder, which gains a substantial disk with a radius of approximately 100 AU, or by the central star. The accretion rate of the central star remains variable with several phases of enhanced accretion, though the peak accretion rates in these phases do not exceed a few times $10^{-5} M_{\odot} yr^{-1}$ except for around $t = 15,500$ years, when a tidal tail connects between the two stars and the accretion rate peaks at $1.5 \cdot 10^{-4} M_{\odot} yr^{-1}$. However, this peak does not have characteristics similar to FUor outbursts. The accretion rate around this time is highly oscillating between $10^{-5} M_{\odot} yr^{-1}$ and $10^{-4} M_{\odot} yr^{-1}$ but increases only by a factor three within one oscillation. The rise and decay times are approximately equal. In contrast, FUors typically have much shorter rise times than decay times and the increase in the accretion rate spans several orders of magnitudes.

There is a large drop in the accretion rate, as seen in Figure 4.6, after the original disk has been cleared around 19,000 years into the simulation.

One should note that the current version of the code may not be well-suited for following the long-term evolution of a binary system for several reasons: While the intruder can gain a circumstellar disk, it cannot accrete any matter from that disk. Thus, not only the matter that would in fact be removed from the disk due to accretion remains in the disk, it is also not possible to gain any information on the accretion rate of the intruder. As mentioned in Chapter 3, the luminosity of the intruder is not taken into account either, even though the intruder may be the more luminous star.

These caveats, however, will most likely not change the general picture observed, and are very unlikely to alter the major result from this model, the FUor outburst.

4.3.4 Fragments captured by intruder

In two models (R4 and P6) the fragment is captured and destroyed by the intruder. Most of its mass is accreted onto the intruder's disk. The linear momentum of the intruder and the captured material partly cancels. Therefore the intruder is significantly slowed down. In the retrograde model (R4) the transferred momentum is much larger, as the fragment and the intruder move in opposite directions at first. As a consequence, the intruder is caught and stays in a highly eccentric orbit.

It is quite likely that the accretion of the fragment by the intruder causes a luminosity burst. Unfortunately, with the current code it is not possible to infer the accretion rate or luminosity of the intruder to confirm this and

quantify the change in accretion rate. We plan to include an accretion scheme for the intruder in future simulations.

4.3.5 State of the disk after the encounter

In all of the models the disks around the target star lose mass during the encounter and are truncated, both due to the ejection of fragments and the capture of disk material by the intruder. In general, disk masses and radii after the encounter are higher in the retrograde models. This is mostly because more fragments are ejected in the prograde models. Another factor is that the intruder gains a somewhat larger disk in prograde encounters because of its lower velocity relative to the disk. In most of the models, especially the ones with fragment ejection, fragmentation ceases after the encounter, as the disk is not massive enough any more. However, in Models R2 and R3, in which no fragment is ejected, there is still a significant amount of fragmentation happening after the encounter.

Table 4.1: Overview of the simulations

Model	$v_{r,0}$ (km/s)	$v_{\phi,0}$ (km/s)	ϕ_0 (deg)	expected periastron[a] (AU)	actual periastron (AU)	Fragment ejected?
P1	-1.8	0.5	90	473	412	yes
P2	-2.1	0.7	90	704	659	yes
P3	-1.9	0.6	90	606	556	yes
P4	-1.7	0.45	90	410	338	yes (2)
P5	-1.6	0.4	90	343	282	yes
P6	-1.8	0.5	180	473	391	yes (2)
P7	-1.8	0.5	270	473	467	yes (2)
P8	-1.8	0.5	0	473	495	yes
R1	-1.8	-0.5	90	473	466	yes
R2	-2.1	-0.7	90	704	700	no
R3	-1.9	-0.6	90	606	601	no
R4	-1.7	-0.45	90	410	397	no
R5	-1.6	-0.4	90	343	330	no
R6	-1.8	-0.5	180	473	486	no
R7	-1.8	-0.5	270	473	423	no
R8	-1.8	-0.5	0	473	384	no

[a] Calculated analytically treating the disk-star system as a point mass.
The columns show, from left to right, the model identifier (the names of prograde models start with P, the ones of retrograde models with R), radial and azimuthal components of the initial velocity of the intruder $v_{r,0}$ and $v_{\phi,0}$, the initial azimuthal position of the intruder ϕ_0, expected and actual periastron radius and whether fragments have been ejected during the simulation.

Table 4.2: Properties of ejected fragments

Model	M_{frag} (M_{Jup})	M_{Hill} (M_{Jup})	v_s (km/s)	v_i (km/s)	$E_{kin}/\|E_{pot}\|$	fragment origin
P1	24	45	1.67	2.20	3.32 (CM)	D
P2	21	40	1.18	2.80	2.93 (S)	D
P3	23	41	1.37	2.56	4.54 (S)	D
P4	25	44	1.46	1.65	1.75 (CM)	D
	9	13	1.20	2.08	3.03 (S)	T
P5	13	23	1.39	1.27	1.38 (CM)	T
P6 [a]	9	21*	1.39	2.47	2.94 (S)	T
	5	14*	1.22	2.26	2.06 (S)	T
P7	10	23	1.88	2.15	2.92 (CM)	D
	10	24	1.46	2.21	3,25 (CM)	T
P8 [b]	5	13	1.11	2.64	2.22 (S)	T
R1	10	25	2.13	3.33	7.32 (CM)	D

* Hill radii of the fragments overlap.

[a] Velocities determined at $r \approx 2,000$AU.

[b] Velocities determined at $r \approx 2,500$AU.

The columns show, from left to right, the fragment mass M_{frag}, the mass located inside the fragment's Hill radius M_{Hill}, the velocity of the fragment relative to the disk central star v_s and the intruder v_i, the ratio of kinetic to potential energy in the reference frame in which this ratio is the lowest with the reference frame indicated in brackets (CM=center of mass system, S=central star), and the fragment origin, where D indicates that the fragment formed inside the disk before the encounter and T marks fragments formed in tidal arms during the encounter.

Chapter 5

Conclusion

The effect of stellar encounters on the dynamics of massive protostellar disks prone to gravitational fragmentation was examined using grid-based two-dimensional hydrodynamics simulations. In particular, we consider a star of $0.63\,M_\odot$ surrounded by a $0.25\,M_\odot$ disk which is initially unstable and fragmenting. It was found that in prograde encounters the ejection of fragments from the disk is very likely. In all simulations involving prograde encounters, at least one fragment was ejected. Half of the ejected fragments formed within the disk before the encounter, while the other half formed in tidal tails during the encounter. Ejected fragments formed in the disk have masses in the brown dwarf regime and are likely to form free-floating brown dwarfs. The fragments formed in tidal tails in contrast have lower masses (5 - 13 M_{Jup}). Depending on whether they still accrete from the mass reservoir located inside their Hill radii, they might remain in the planetary mass regime.

All ejected fragments have a significant amount of mass (13-45 M_{Jup}) located within their Hill radius. A part of this mass might be accreted by the fragments and form proto-brown dwarf disks, which have been observed around young brown dwarfs.

Ejections in retrograde encounters are very unlikely. Only one of the eight performed simulations showed such an ejection. In that case, the intruder passes the fragment very closely. In another retrograde simulation, the close passage of the intruder accelerates a fragment onto the disk central star, causing an increase in accretion rate resembling FU Orionis (FUor) type outbursts both in magnitude and shape. Though spectacular, this process is rare and therefore not suited to serve as a general mechanism to explain FUor outbursts.

After the encounter, the disks are truncated in all of the simulations, as reported in other studies of encounters. In general, this effect is higher for prograde models. In the majority of the simulations, fragmentation ceases

after the encounter, as the disk has lost too much mass.

Due to the two-dimensionality of our code, the study is restricted to coplanar encounters. However, these encounters are expected to have the highest effect on the disk evolution. Another restriction is that due to the logarithmic cell spacing in the radial direction resolution decreases as the fragments move away from the central star. A few fragments disperse once they reach a distance of $> 3000\,\mathrm{AU}$ from the central star, as the cell size becomes larger than the size of the fragments. It is likely that these fragments would survive if the grid solution were higher. Simulations with increased resolution are planned for the future.

Appendix A

Testing

A.1 Integration routine

The two-body problem is used to test whether the code is working and accurately reproducing the behavior of a particle in a central potential: A particle with negligible mass is launched at 10 AU distance from a solar-mass star. The initial velocity of the particle is parallel to $\hat{e}_\varphi$ and its magnitude is varied ranging from 0.5 to 1.7 times the circular orbital velocity v_c. The resulting trajectories are plotted in Figure A.1. As expected, an initial velocity $v_0 < v_c$ corresponds to an elliptical orbit with the starting point being the apoapsis, while for $v_c < v0 < v_{esc}$ the starting point becomes the periapsis. An initial velocity that is exactly the escape velocity $v_{esc} = \sqrt{2}v_c$ results in a parabolic trajectory and initial velocities higher than the escape velocity in hyperbolic orbits.

The solution of the integration routine is then compared to the solution obtained through Kepler's equation. As a transcendental equation, Kepler's equation has to be solved numerically. This is done using the Newton-Raphson method. I chose the termination condition for the Newton-Raphson method such that the estimated error in φ is at most of order 10^{-12} which is several orders of magnitude below the error from the numerical integration routine. In addition, as the solution of Kepler's equation only depends on the initial conditions and not on any iterative steps in between, there is no cumulative error that is introduced. Therefore, the solution obtained this way is clearly reliable enough for determining the error of the integration routine. Figure A.2 shows the error of the integration routine for various elliptical orbits over 1000 orbits. The error increases for orbits with higher eccentricity, but even for the highest eccentricity considered ($v_0 = 0.5v_c, e = 0.75$) the error after 1000 orbits is only 0.2 %.

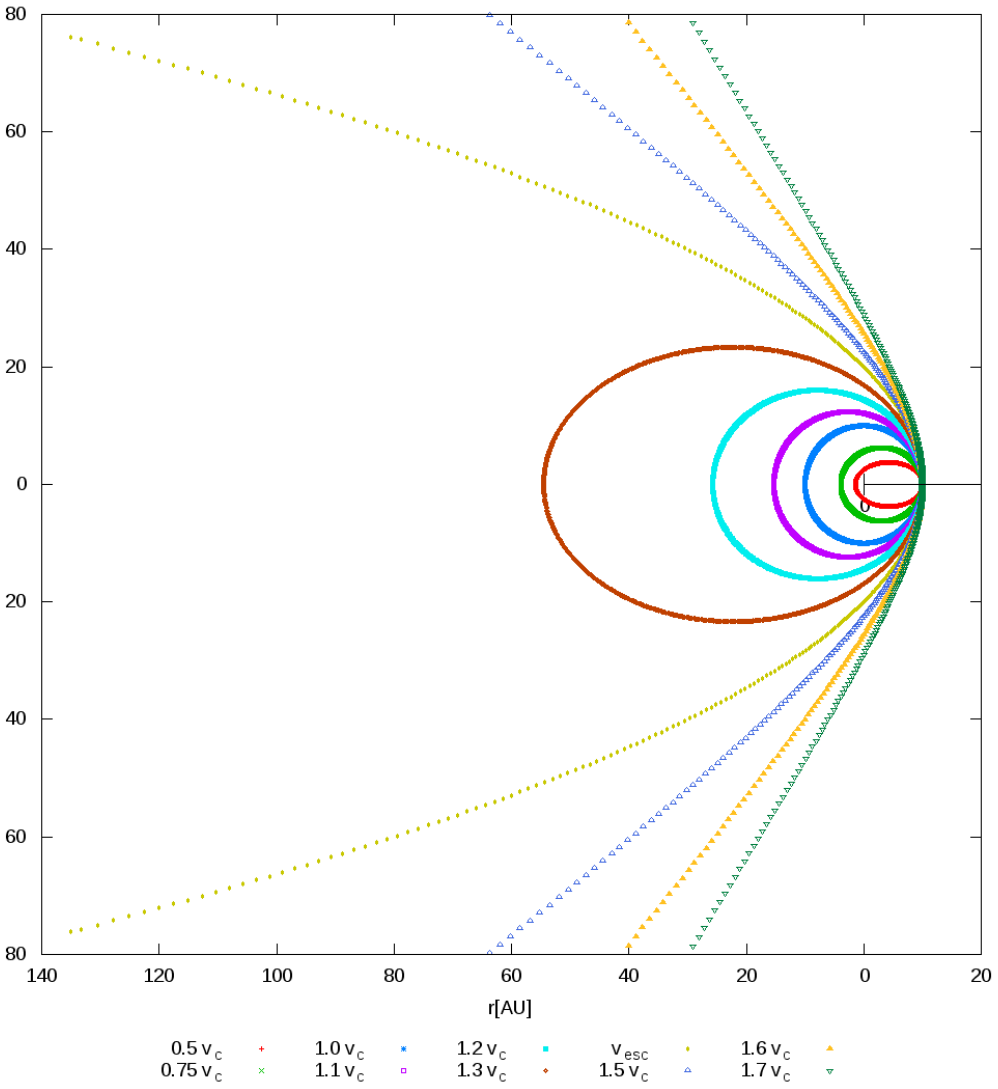

Figure A.1: Trajectories of the particle with different initial velocities.

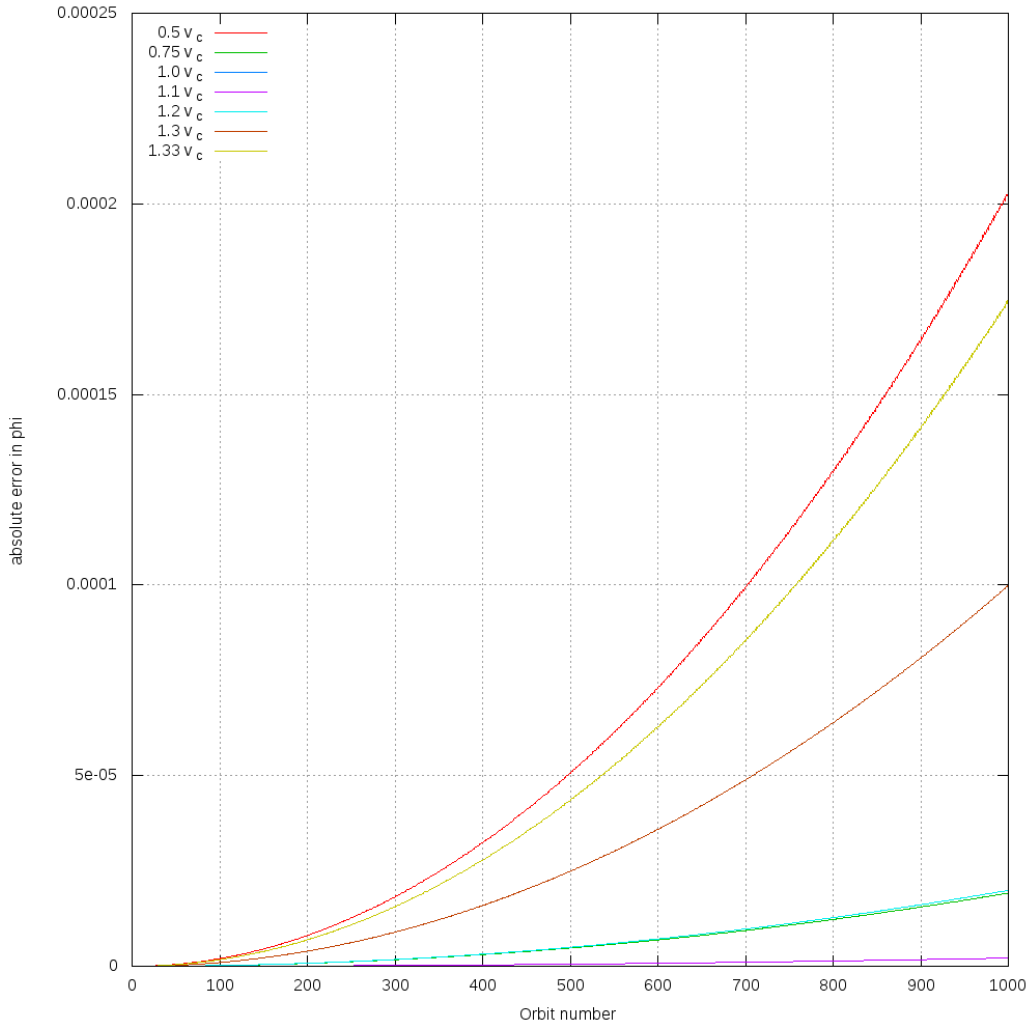

Figure A.2: Error of the angular position $\Delta\varphi$ from the integration routine compared to the numerical solution of Kepler's equation.

It is important to note that coupling the routine to the hydrodynamics code can increase the error drastically, as the force acting on the intruder is then only calculated once per hydrodynamical timestep. However, for the hyperbolic trajectories considered in this work, the error is estimated to stay below 1 %.

A.2 Acceleration of intruder due to the disk

To demonstrate that the routine for calculating the acceleration of the intruder due to the disk is producing accurate results, I tested the routine on a 1/r surface density disk, for which the disk potential and the gravitational acceleration have a simple analytic form (Binney and Tremaine, 1987, p. 76f). As the routine does not take into account any mass inside the sink cell, the acceleration of a point mass with the mass located inside the sink cell is subtracted from the analytical solution for comparison with the numerical solution. In the full simulations, the material inside the sink cell is treated as a point mass and added to the mass of the star. Figure A.3 shows that the numerical solution agrees well with the analytical solution throughout most of the computational domain, with significant deviations only close to the boundaries. In fact, the relative error stays below 1 % for radii between 30 AU and $\approx$ 3000 AU. The reason for the strong deviations close to the boundary is that the analytical solution is for an infinite disk, while for the numerical solution the disk is cut off at the inner and outer boundary. However, in none of our simulations the intruder comes close enough to the boundaries for these effects to be. However, in our simulations the intruder never approaches the boundaries close enough for these effects to become relevant.

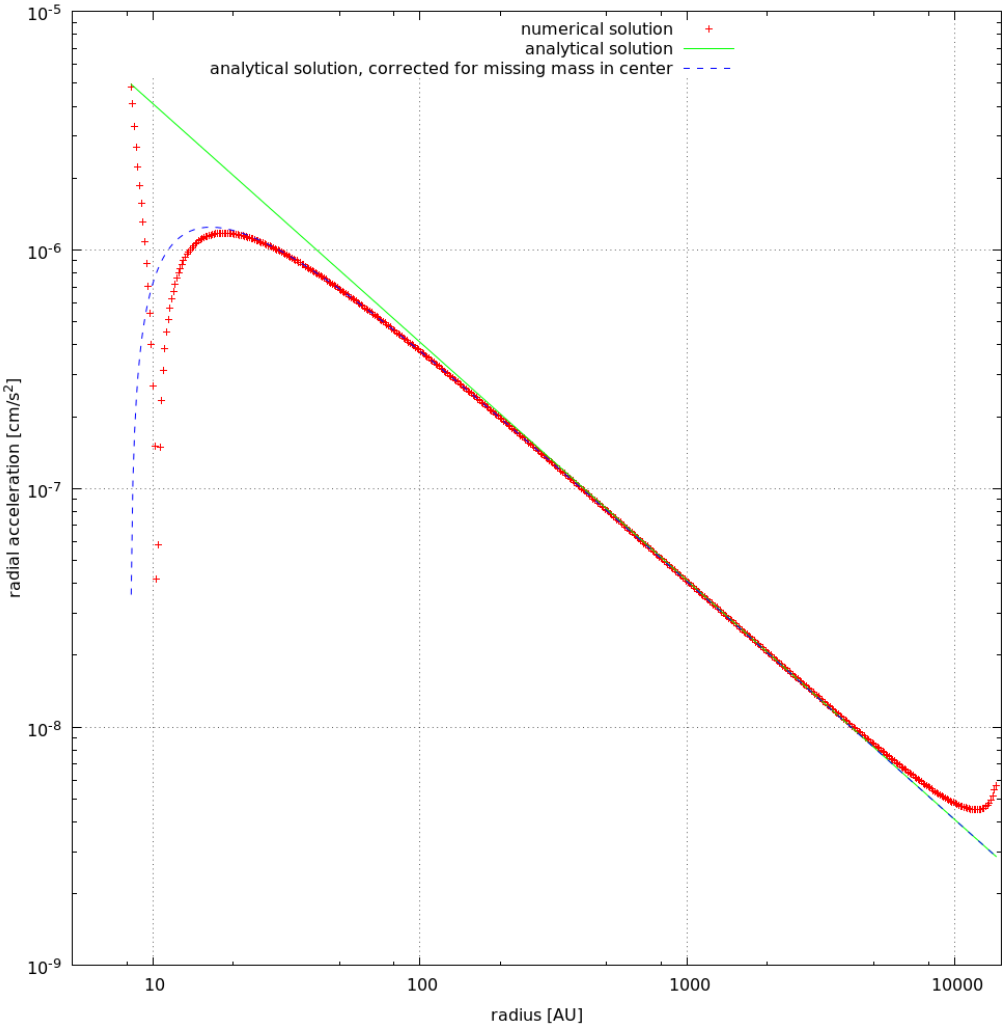

Figure A.3: Comparison of the radial gravitational acceleration towards the center of a 1/r surface density disk, calculated analytically and with the routine used in our code.

Bibliography

Audard, M., Ábrahám, P., Dunham, M. M., Green, J. D., Grosso, N., Hamaguchi, K., Kastner, J. H., Kóspál, Á., Lodato, G., Romanova, M. M., Skinner, S. L., Vorobyov, E. I., and Zhu, Z.: 2014, *Protostars and Planets VI* pp 387–410

Baraffe, I. and Chabrier, G.: 2010, *A&A* **521**, A44

Baraffe, I., Vorobyov, E., and Chabrier, G.: 2012, *ApJ* **756**, 118

Basu, S. and Vorobyov, E. I.: 2012, *ApJ* **750**, 30

Bate, M. R.: 2012, *MNRAS* **419**, 3115

Binney, J. and Tremaine, S.: 1987, *Galactic Dynamics*, Princeton University Press

Boss, A. P.: 2001, *ApJ* **563**, 367

Chabrier, G., Johansen, A., Janson, M., and Rafikov, R.: 2014, *Protostars and Planets VI* pp 619–642

Da Rio, N., Gouliermis, D. A., and Gennaro, M.: 2010, *ApJ* **723**, 166

Forgan, D. and Rice, K.: 2009, *MNRAS* **400**, 2022

Forgan, D. and Rice, K.: 2010, *MNRAS* **402**, 1349

Gammie, C. F.: 2001, *ApJ* **553**, 174

Hartmann, L. and Kenyon, S. J.: 1996, *ARA&A* **34**, 207

Hillenbrand, L. A.: 2009, in E. E. Mamajek, D. R. Soderblom, and R. F. G. Wyse (eds.), *IAU Symposium*, Vol. 258 of *IAU Symposium*, pp 81–94

Johnson, B. M. and Gammie, C. F.: 2003, *ApJ* **597**, 131

Klahr, H. and Kley, W.: 2006, *A&A* **445**, 747

Kratter, K. M., Matzner, C. D., Krumholz, M. R., and Klein, R. I.: 2010a, *ApJ* **708**, 1585

Kratter, K. M., Murray-Clay, R. A., and Youdin, A. N.: 2010b, *ApJ* **710**, 1375

Longair, M. S.: 2011, *High Energy Astrophysics*, Cambridge University Press

Luhman, K. L.: 2012, *ARA&A* **50**, 65

Muñoz, D. J., Kratter, K., Vogelsberger, M., Hernquist, L., and Springel, V.: 2015, *MNRAS* **446**, 2010

Offner, S. S. R., Clark, P. C., Hennebelle, P., Bastian, N., Bate, M. R., Hopkins, P. F., Moraux, E., and Whitworth, A. P.: 2014, *Protostars and Planets VI* pp 53–75

Pfalzner, S.: 2008, *A&A* **492**, 735

Pfalzner, S., Tackenberg, J., and Steinhausen, M.: 2008, *A&A* **487**, L45

Press, W. H., Teukolsky, S. A., Vetterling, W. T., and Flannery, B. P.: 2007, *Numerical Recipes - The Art of Scientific Computing*, Cambridge University Press, 3rd edition

Reipurth, B. and Clarke, C.: 2001, *AJ* **122**, 432

Rice, W. K. M., Armitage, P. J., Bate, M. R., and Bonnell, I. A.: 2003, *MNRAS* **339**, 1025

Rosotti, G. P., Dale, J. E., de Juan Ovelar, M., Hubber, D. A., Kruijssen, J. M. D., Ercolano, B., and Walch, S.: 2014, *MNRAS* **441**, 2094

Shakura, N. I. and Sunyaev, R. A.: 1973, *A&A* **24**, 337

Shen, S. and Wadsley, J.: 2006, *ApJ* **651**, L145

Shen, S., Wadsley, J., Hayfield, T., and Ellens, N.: 2010, *MNRAS* **401**, 727

Slesnick, C. L., Hillenbrand, L. A., and Carpenter, J. M.: 2008, *ApJ* **688**, 377

Stamatellos, D. and Whitworth, A. P.: 2009, *MNRAS* **392**, 413

Thies, I., Kroupa, P., Goodwin, S. P., Stamatellos, D., and Whitworth, A. P.: 2010, *ApJ* **717**, 577

Toomre, A.: 1964, *ApJ* **139**, 1217

Vorobyov, E. I.: 2013, *A&A* **552**, A129

Vorobyov, E. I. and Basu, S.: 2005, *ApJ* **633**, L137

Vorobyov, E. I. and Basu, S.: 2006, *ApJ* **650**, 956

Vorobyov, E. I. and Basu, S.: 2010a, *ApJ* **714**, L133

Vorobyov, E. I. and Basu, S.: 2010b, *ApJ* **719**, 1896

Vorobyov, E. I. and Basu, S.: 2015, *ApJ* **805**, 115

Whitworth, A. P. and Zinnecker, H.: 2004, *A&A* **427**, 299

Zhu, Z., Hartmann, L., Nelson, R. P., and Gammie, C. F.: 2012, *ApJ* **746**, 110